

SIMULATION ON TEMPERATURE IN CHANNEL OF THREE-PHASE INDUCTION CHANNEL FURNACE FOR STEEL MELTING USING COMSOL MULTIPHYSICS AND TAGUCHI METHOD

Myong-Hae Kwon, Hak-Myong Song and Won-Chol Yang 

Department of Mechanical Engineering, Kim Chaek University of Technology, 60 Kyogu, Pyongyang, Democratic People's Republic of Korea

Copyright © 2023 American Foundry Society
<https://doi.org/10.1007/s40962-023-00986-y>

Abstract

Induction channel furnaces (ICF) are widely used for melting, holding and casting metals and alloys in many processing industries because it has higher overall efficiency, lower electric power consumption and operation costs, better degassing and homogenization of the melt, lower oxide and slag formation than other induction furnaces. However, thermal stresses in the refractory lining caused by high temperature and flow of molten metal may cause its premature erosion of the lining and, failure of the inductor, and so it has difficulty to repair the furnace. In addition, the furnace for steel melting often experiencing shortened operating life and quicker needs for a repair cycle due to high temperature of molten metal and severe erosion of lining, so it is little used. In this paper, we

propose a new type of channel of three-phase ICF for steel melting, and study temperature distribution of the channel by coupled simulation for the electromagnetic-heat-fluid using COMSOL Multiphysics 5.4 and Taguchi method. Simulation result demonstrates that maximum local superheating temperature (28.6K) of channel in the three-phase ICF for steel melting is as low as that (27K) of blowing channel in the two phase ICF, so it can be satisfactorily employed for steel melting.

Keywords: induction channel furnace, coupled simulation, COMSOL Multiphysics, Taguchi method

Introduction

Induction channel furnace (ICF) has been widely utilized for melting, refining and holding of metal owing to its advantages such as higher power factor, less electric power consumption and less stirring of molten metal because magnetic induction line follows the closed core.

In general, the ICF composes of the induction units with iron core, inductor and channel, and the molten metal bath. The induction units are assembled in furnace body and are separated when the furnace is repaired. If an electric current flows through inductor, very large induced current flows through channel due to electromagnetic induction phenomenon. Then the channel is heated by Joule heat from the induced current, and this heat makes the metal

molten through continuous transfer into the molten metal bath. Therefore, the temperature of channel is higher than that of the molten metal bath during melting, and it shortens repair cycle of the furnace due to severely erosion of lining of the channel. Especially, the temperature of liquid steel is high and erosion of lining is very severe, so it is subject to restriction on melting in ICF.¹

In order to solve these problems, various kinds of methods developed.

Webster Jr² developed a new technique, using permanent ceramic loop forms produced by the proprietary Blasch Precision Ceramics process and Calamari³ introduced that the induction furnace with incorporated channel was convenient to fabricate and have good electrical characteristics and low power consumption and productivity.

Duca illuminated thermodynamics of inductor lining wear, channel plugging, lining saturation and mechanism of

saturation,⁴ and discussed the mechanism of lining wear in an inductor lined with a spinel-bonded magnesia lining and melting ductile-based iron.⁵

Nowadays many researchers numerically simulated heat-and-mass transfer in various furnaces using different software. Bara⁶ discussed the computation methods and experimental techniques available and observed that the finite element method is very much efficient method for the modeling.

Ghojel et al.^{7,8} developed a such a tool using a thermal modeling software and unidirectional axial channel flow speeds of the melt that are estimated from analysis based on the first-law of thermodynamics. This analysis reduces the cost, complications and uncertainties associated with coupled multiple field analysis approach. The results of the analysis show reasonable correlation with reported flow data and a comprehensive set of scenarios can be devised on the basis of the developed approach to simulate start-up, transient operation and steady-state operation of double-loop channel induction furnaces.

Alferenok et al.⁹ used the ANSYS Multiphysics and ANSYS CFX software packages to numerically simulate the effect of the channel shape and the circuit of the inducing windings of induction coils on the heat-and-mass transfer in the double induction unit of a channel furnace for making cast iron. They found that the heat-and-mass transfer in an ICF substantially depends on the shape and sizes of the throat of the central channel and more weakly depends on the circuit of the induction coils. With the developed models, they can determine the optimum sizes of the throat of the central channel to achieve the minimum superheating of the melt.

The superheat is the difference between the maximum and minimum temperature in the channel. High superheat of the channel may cause the premature erosion of the lining of channel and failure of the inductor, so it is very important.

Pavlovs et al.¹⁰ and Alferenok et al.⁹ determined maximum temperature T_{\max} and its position α through the simulation and experiment of several single and double-loop channel, and suggested the method of improvement in the channel structure of ICF. The maximum local superheating temperature in some channel of one phase ICF is 32–48K¹⁰ and that in some channel of two phase ICF is 27–33K.⁷ Especially some double-loop channel of two phase ICF is sufficiently used for steel melting because its repair cycle is long due to 27–33 K of maximum local superheating temperature. Baake et al.^{10–18} simulated heat-and-mass transfer in ICF using large eddy simulation (LES) approach of fluid flow and gave further study to modeling and simulation coupled with electromagnetic-heat-fluid dynamic process using LES model. The LES model of turbulence

provides more precise results of HD and temperature computations versus k-model and the long term modeling (several hundred seconds of flow time) is necessary to reach definite stabilization of thermal field distribution in symmetrical ICF because of low frequency oscillations of T_{\max} value and position including its transition from one branch of the channel to another.

Podoltsev et al.¹⁹ suggested the method to predict the defect in ICF by determine of quantitative relationship between the impedance of inductor and leakage of molten metal experimentally. They considers one of the methods for diagnosing the state of the lining of an induction channel furnace. The method is based on comparison of the measured values of the complex impedances of the furnace inductor with a defect-free lining and lining with defects. In this case, only defects leading to a change in the electrical parameters of the secondary liquid-metal circuit are taken into account. And using two electric equivalent circuits of the inductor, the analytic expressions and graphics dependencies determining a quantitative relationship between the parameters of the liquid-metal circuit and the inductor parameters measured in practice are obtained. In the case of small changes in these parameters (less than 10 %), a linear relationship between their increments is 34 used with the determination of a sensitivity matrix A, which clearly demonstrates the presence of strong or weak coupling between the perturbed values of the secondary circuit parameters and the inductor ones. The technique for calculating the increments of equivalent inductor parameters as a function of increments of the parameters of the secondary liquid-metal circuit is proposed. The use of this technique allows to develop the database for various types of lining defects for a given furnace and on its basis predict the state of its lining by means of periodic measurements of the inductor parameters

Lüdtke et al.²⁰ provided the numerical simulation of the frequency dependence with regard to the electrical efficiency of induction furnaces. Singh et al.²¹ and Bhat et al.²² performed 2D axis symmetric induction furnace analysis using COMSOL multiphysics software. They shows how to solve the induction heating problem in the induction furnace with complex geometry.

Some researchers studied electromagnetic and temperature field distribution in cold crucible induction furnace,²³ vacuum induction furnace²⁴ by heat transfer coupled with induction heating module of COMSOL Multiphysics.

In this paper, a new type channel of three-phase ICF for steel melting is proposed, the method of the thermal and electromagnetic modeling in COMSOL Multiphysics 5.4 is described, and its temperature distribution and flow characteristics are discussed.

Simulation for the Three-Phase ICF Using COMSOL Multiphysics 5.4 Based on Orthogonal Array

3D Geometry of the Three-Phase ICF for Steel Melting

ICF consists of molten metal bath and induction unit included with iron core, inductor and channel.

Local superheating temperature reaches below to 27–33 K because of fast flow velocity (0.22–0.23 m/s) of the molten metal in channel of ICF, in which double-loop inductor is widely utilized for melting steel.

If one three-phase induction unit is fixed to furnace body and ICF are reconstructed to three-phase slope type, they will lead to decrease in electrical unbalance and rise of power, ease in repair of furnace.

We propose a channel of three-phase ICF as shown in Figure 1a and b, and set it with a certain setting angle on the molten metal bath, so make it utilize for steel melting.

Simulation Method Using COMSOL Multiphysics 5.4

Joule heat generation due to electromagnetic induction, the heating and melting of the channel and flow of the molten metal caused in ICF are not isolated from each other, and they are coupled with several correlated physical field. In other words, induced current caused by electromagnetic induction generates the Joule heat, and the heat transfer leads the heating and melting of the channel. Also Ampere force and gravity lead to the flow of the molten metal, and it varies the temperature distribution affected on lifetime of the furnace. Because the heating and melting of the channel

by mutual combination of electromagnetic, temperature and fluid field, when we simulate by combination of calculation result of individual fields, the melting process in ICF could not be explained satisfactorily.

COMSOL Multiphysics 5.4, coupled simulation software of multiphysics field analyzes heating process of metal by electromagnetic field and Joule heat using Heat Transfer/Electromagnetic Heating/ Induction Heating analysis module. This analysis module solves by couple with electromagnetic field module 'Magnetic Field (mf)' and heat transfer module in solid 'Heat Transfer in Solids (ht)' using function of Multiphysics, and outputs the distribution of electromagnetic field and temperature according to time. The latent heat and phase transition temperature interval are given and the output value is electromagnetic field and temperature distribution at that time.

After all the metal in the channel changes into liquid, the calculation for turbulent flow field should be carried out due to convection caused by Ampere force and gravity acting molten metal. So, the characteristic of motion of the molten metal due to Ampere force and gravity is analyzed.

The calculation equation of Ampere force is as follows:

$$\begin{aligned} \mathbf{F}_m &= \text{Im}\mathbf{J} \times \text{Im}\mathbf{B} = \sigma \text{Im}\mathbf{E} \times \text{Im}\mathbf{B} = -\sigma\omega \text{Im}(j\mathbf{A}) \times \text{Im}\mathbf{B} \\ &= -\sigma\omega \text{Re}\mathbf{A} \times \text{Im}\mathbf{B}. \end{aligned}$$

Eqn. 1

where \mathbf{J} is the current density vector (A/m^2), \mathbf{B} is the magnetic induction vector (T), \mathbf{E} is the electric field strength vector (V/m), σ is the conductivity of material (S/m), ω is the angular frequency of input alternating current (s^{-1}), and \mathbf{A} is the magnetic potential (Wb/m).

Therefore, to calculate the Ampere force acted in unit volume around any point, it is need to find the real part of

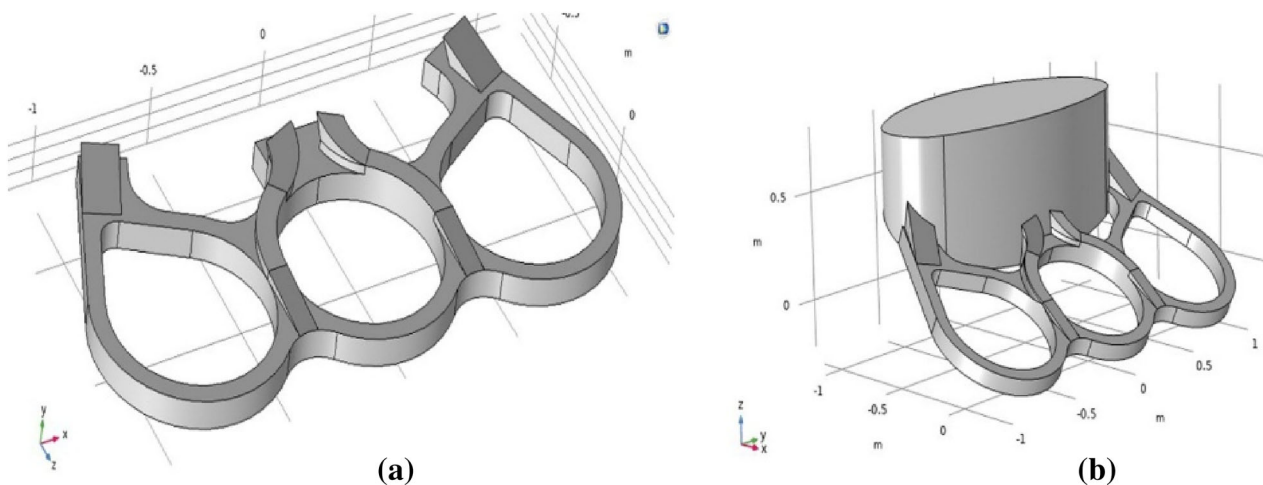


Figure 1. 3D-geometry of the channel and molten metal bath of the three-phase ICF: (a) Channel geometry, (b) Placing position of channel and molten metal bath.

complex vector magnetic potential and imaginary part of complex magnetic fluid vector of that point.

AC/DC/Magnetic Field (mf) analysis module outputs the magnetic potential and magnetic fluid vector in the form of complex number at the point of space, they are as follows:

$$\begin{cases} \mathbf{A} = (A_x, A_y, A_z), A_x = A_{x1} + jA_{x2}, A_y = A_{y1} + jA_{y2}, A_z = A_{z1} + jA_{z2}, \\ \mathbf{B} = (\text{mf.B}_x, \text{mf.B}_y, \text{mf.B}_z), \\ \text{mf.B}_x = B_{x1} + jB_{x2}, \text{mf.B}_y = B_{y1} + jB_{y2}, \text{mf.B}_z = B_{z1} + jB_{z2}. \end{cases} \quad \text{Eqn. 2}$$

In the above equation, the values of real and imaginary parts at a point are the values in any topology of sinusoidal wave, so the calculation result from Eqn. 2 is not accurate value.

Therefore, the calculation of Ampere force should be calculated as average of the values changing along with sinusoidal wave. That is, the magnitude equals to the average value and its sign equals to the sign at the considering point.

At that time, while considering that half cycle average value of the function $f(t) = f^{\max} \sin(\omega t)$ with cycle T is $\frac{2}{\pi} f^{\max}$, the calculation result of Ampere force is as follow:

$$\begin{cases} \mathbf{F}_m = -\sigma\omega\bar{\mathbf{A}} \times \bar{\mathbf{B}}, \\ \bar{\mathbf{A}} = \frac{2}{\pi} \left(\text{sign}(A_{x1})A_x^{\max}, \text{sign}(A_{y1})A_y^{\max}, \text{sign}(A_{z1})A_z^{\max} \right), \\ A_x^{\max} = (A_{x1}^2 + A_{x2}^2)^{1/2}, A_y^{\max} = (A_{y1}^2 + A_{y2}^2)^{1/2}, A_z^{\max} = (A_{z1}^2 + A_{z2}^2)^{1/2}, \\ \bar{\mathbf{B}} = \frac{2}{\pi} \left(\text{sign}(B_{x2})B_x^{\max}, \text{sign}(B_{y2})B_y^{\max}, \text{sign}(B_{z2})B_z^{\max} \right), \\ B_x^{\max} = (B_{x1}^2 + B_{x2}^2)^{1/2}, B_y^{\max} = (B_{y1}^2 + B_{y2}^2)^{1/2}, B_z^{\max} = (B_{z1}^2 + B_{z2}^2)^{1/2}. \end{cases} \quad \text{Eqn. 3}$$

In the case of stationary process, the velocity field of the liquid metal is calculated by using magnetic field analysis module and liquid flow analysis module Fluid Flow/Single-Phase Flow/Turbulent Flow/Turbulent Flow, $k - \varepsilon$ (spf). Here, temperature used in analyzing magnetic field and fluid field utilize the calculation result of thermal conduction analysis module in the liquid, Heat Transfer in Fluids (ht), and gravity and Ampere force set to Eqn. 3 obtained from the calculation result of magnetic field is input as the force lead to fluid flow.

For the geometry of three-phase ICF consisted of channel and molten metal bath shown in Figure 1, the simulation is performed.

Figure 2 shows the finite element model for multiphysics field-coupled simulation of channel of three-phase ICF.

The constructed mesh consists of 77 383 domain elements, 10 546 boundary elements and 2 062 edge elements, and the calculation region is spherical space with radius of 3 m.

The boundary condition $\{A\} = 0$ Wb/m is set to the boundary of the calculation region.

Assuming that industrial pure iron is melted, the values of material properties are as follows:

Input frequency: $f = 60$ Hz, input current: $I = 400$ A, voltage: $U = 450$ V, number of turns of inductor: $N = 31$, sectional area of inductor coil: $S = 1.5 \times 10^{-4}$ m², solidus temperature: $T_m = 1811.15$ K, latent heat: $L = 695.5$ kJ/kg, temperature interval of phase transition: $\Delta T = 10$ K, Curie point: $T_{\text{curie}} = 1043$ K, coefficient of specific resistance: $\alpha = 0.0065$, relative permeability at Curie point and over: $\mu_r = 80$.

The other values of material properties have the default values provided by COMSOL Multiphysics 5.4. Because the early erosion and expansion of refractory lining of the channel occurring in the ICF are produced by high and local superheating and flow of the molten metal in the channel, the simulation have been done until tapping since metal melted completely, i.e., until 0.5 h.

Design of Experiment for Simulation Based on Taguchi's Orthogonal Array

In this study, four design parameters at three levels are used to simulate the local superheating behavior; hence, the simulation experiments are conducted based on the Taguchi's standard orthogonal array (OA) $L_9(3^4)$ (Table 1). Four design parameters for three-phase ICF are assigned to each column of the OA $L_9(3^4)$. First column is assigned to type of channel (A), second column to dimensions of channel (B), third column to existence of protruding part (C), and the fourth to setting angle of channel (D). The design parameters at each level are shown in Table 2.

We calculate the maximum and minimum temperatures, and absolute and relative local superheating temperatures of the channel depending on time (0.1, 0.2, 0.3, 0.4 and 0.5 hours) in molten metal from the simulation results.

Results and Discussion

Simulation Experiment Results Based on the OA $L_9(3^4)$

We conducted the simulation experiments based on the OA $L_9(3^4)$

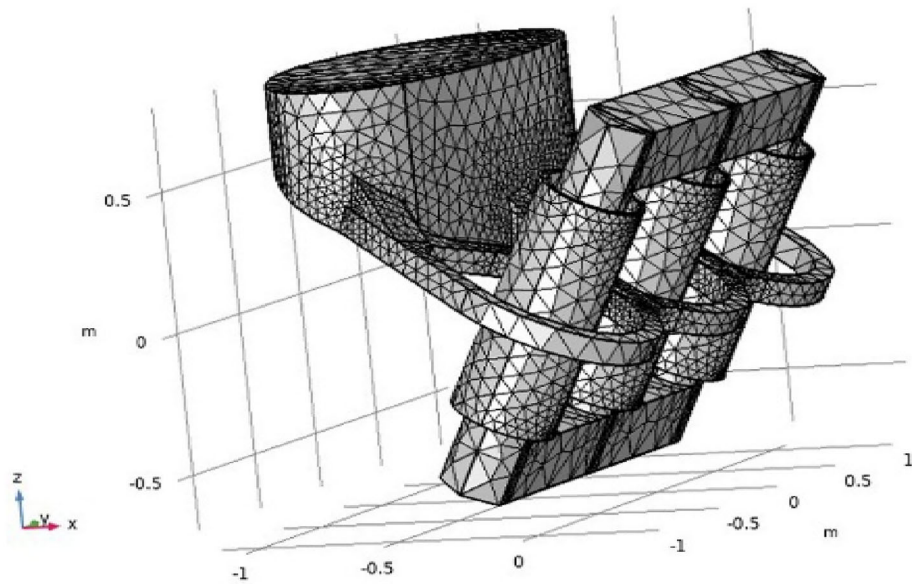


Figure 2. Finite element model of calculation object.

Table 1. Taguchi OA $L_9(3^4)$ nnnh

Trial no.	A	B	C	D
1	1	1	1	1
2	1	2	2	2
3	1	3	3	3
4	2	1	2	3
5	2	2	3	1
6	2	3	1	2
7	3	1	3	2
8	3	2	1	3
9	3	3	2	1

Table 2. List of Control Factors (or Design Parameters for Three-Phase ICF) for Taguchi Simulation Experiment

Level	Factors			
	Type of channel (A)	Dimensions of channel (B)	Existence of protruding part (C)	Setting angle of channel (D)
1	Elliptic	65×90 mm ²	Yes	30°
2	Circular	85×90 mm ²	No	0°
3	Square	65×70 mm ²	No	90°

Tables 3, 4, 5, 6, 7, 8, 9, 10, 11 show the maximum and minimum temperatures, and absolute and relative local superheating temperatures of the channel depending on time according to each simulation experiment condition.

Figures 3, 4, 5, 6, 7, 8, 9, 10, 11 show the temperature distribution of the molten metal at the time $t = 0.5h$ according to each simulation experiment condition.

In the above tables, the absolute local superheating temperature dT is the difference of maximum and minimum temperature in channel and the relative local superheating temperature δ is $dT/T_{\max} \cdot 100$.

All the simulation experiment results (relative local superheating temperatures) based on the OA $L_9(3^4)$ are listed in Table 12.

Analysis Result of Simulation Experiments and Discussion

To analyze the simulation experiment result, S/N ratios for each of the nine trial conditions are calculated. The S/N ratio according to i th trial (condition) is calculated by the lower-the better formula because the relative local superheating temperature is a cost property (the lower-the better property). The formula is as follows:

$$SNR_i = -10 \lg \left(\frac{1}{5} \sum_{k=1}^5 \delta_{ik}^2 \right) \quad \text{Eqn. 4}$$

Table 3. Maximum and Minimum Temperatures, Absolute and Relative Local Superheating Temperatures Depending on Time According to $A_1B_1C_1D_1$

Time t, h	0	0.1	0.2	0.3	0.4	0.5
Maximum temperature T_{max} , K	1811.2	1860.1	1881.8	1902.2	1921.4	1939.2
Minimum temperature T_{min} , K	1811.2	1831.5	1854.4	1875.9	1895.9	1914.4
Absolute local superheating temperature dT, K	0	28.6	27.4	26.3	25.5	24.8
Relative local superheating temperature δ , %	0	1.538	1.456	1.383	1.327	1.279

Table 4. Maximum and Minimum Temperatures, Absolute and Relative Local Superheating Temperatures Depending on Time According to $A_1B_2C_2D_2$

Time t, h	0	0.1	0.2	0.3	0.4	0.5
Maximum temperature T_{max} , K	1811.2	1859.8	1881.4	1901.9	1921.3	1939.4
Minimum temperature T_{min} , K	1811.2	1825.8	1847.1	1867.5	1886.6	1904.4
Absolute local superheating temperature dT, K	0	34	34.3	34.4	34.7	35
Relative local superheating temperature δ , %	0	1.828	1.823	1.809	1.806	1.805

Table 5. Maximum and Minimum Temperatures, Absolute and Relative Local Superheating Temperatures Depending on Time According to $A_1B_3C_3D_3$

Time t, h	0	0.1	0.2	0.3	0.4	0.5
Maximum temperature T_{max} , K	1811.2	1938.3	1954.1	1968.6	1982.5	1995.4
Minimum temperature T_{min} , K	1811.2	1805	1819.6	1833.5	1846.8	1859.2
Absolute local superheating temperature dT, K	0	133.3	134.5	135.1	135.7	136.2
Relative local superheating temperature δ , %	0	6.877	6.883	6.863	6.845	6.826

Table 6. Maximum and Minimum Temperatures, Absolute and Relative Local Superheating Temperatures Depending on Time According to $A_2B_1C_2D_3$

Time t, h	0	0.1	0.2	0.3	0.4	0.5
Maximum temperature T_{max} , K	1811.2	1891.7	1916	1938.8	1960.5	1980.9
Minimum temperature T_{min} , K	1811.2	1812.7	1835.7	1857.6	1878.2	1897.6
Absolute local superheating temperature dT, K	0	79	80.3	81.2	82.3	83.3
Relative local superheating temperature δ , %	0	4.176	4.191	4.188	4.198	4.205

Table 7. Maximum and Minimum Temperatures, Absolute and Relative Local Superheating Temperatures Depending on Time According to $A_2B_2C_3D_1$

Time t, h	0	0.1	0.2	0.3	0.4	0.5
Maximum temperature T_{max} , K	1811.2	1901.6	1958.5	2012.4	2062.8	2109.3
Minimum temperature T_{min} , K	1811.2	1866.9	1923.5	1976.9	2026.8	2073
Absolute local superheating temperature dT, K	0	34.7	35	35.5	36	36.3
Relative local superheating temperature δ , %	0	1.825	1.787	1.764	1.745	1.721

Table 8. Maximum and Minimum Temperatures, Absolute and Relative Local Superheating Temperatures Depending on Time According to $A_2B_3C_1D_2$

Time t, h	0	0.1	0.2	0.3	0.4	0.5
Maximum temperature T_{max} , K	1811.2	1877.4	1897.5	1916.6	1934.7	1951.7
Minimum temperature T_{min} , K	1811.2	1816.1	1835.9	1854.8	1872.6	1889.4
Absolute local superheating temperature dT , K	0	61.3	61.6	61.8	62.1	62.3
Relative local superheating temperature δ , %	0	3.265	3.246	3.224	3.210	3.192

Table 9. Maximum and Minimum Temperatures, Absolute and Relative Local Superheating Temperatures Depending on Time According to $A_3B_1C_3D_2$

Time t, h	0	0.1	0.2	0.3	0.4	0.5
Maximum temperature T_{max} , K	1811.2	1867.7	1883.4	1897.9	1911.7	1924.9
Minimum temperature T_{min} , K	1811.2	1810.1	1824.9	1839.2	1852.8	1865.6
Absolute local superheating temperature dT , K	0	57.6	58.5	58.7	58.9	59.3
Relative local superheating temperature δ , %	0	3.084	3.106	3.093	3.081	3.081

Table 10. Maximum and Minimum Temperatures, Absolute and Relative Local Superheating Temperatures Depending on Time According to $A_3B_2C_1D_3$

Time t, h	0	0.1	0.2	0.3	0.4	0.5
Maximum temperature T_{max} , K	1811.2	1864.2	1879.2	1893.4	1907	1919.6
Minimum temperature T_{min} , K	1811.2	1818.5	1833.2	1847.3	1860.6	1873.2
Absolute local superheating temperature dT , K	0	45.7	46	46.1	46.4	46.4
Relative local superheating temperature δ , %	0	2.451	2.448	2.435	2.433	2.417

Table 11. Maximum and Minimum Temperatures, Absolute and Relative Local Superheating Temperatures Depending on Time According to $A_3B_3C_2D_1$

Time t, h	0	0.1	0.2	0.3	0.4	0.5
Maximum temperature T_{max} , K	1811.2	1897.2	1910.8	1923.3	1935.1	1946.3
Minimum temperature T_{min} , K	1811.2	1803.3	1815.5	1827.5	1838.9	1849.6
Absolute local superheating temperature dT , K	0	93.9	95.3	95.8	96.2	96.7
Relative local superheating temperature δ , %	0	4.949	4.987	4.981	4.971	4.968

where $\delta_{ik} = dT_{ik}/T_{ikmax} \cdot 100$ is the relative local superheating temperature at k th time on i th trial.

Using Eqn. 4, the S/N ratios were computed for each of the nine trial conditions.

Table 13 shows the S/N ratios for each of the nine trial conditions.

Table 14 shows the average values of S/N ratios of each factor at the levels 1–3. Table 14 also shows the ranges of S/N ratios (main effects) of each factor. The ranges of S/N ratios are the maximum absolute difference between S/N ratio values at each factor. The larger the range value is, the larger the effect of the factor is.

Figure 12 shows the average values of S/N ratios of each factor at the levels 1–3.

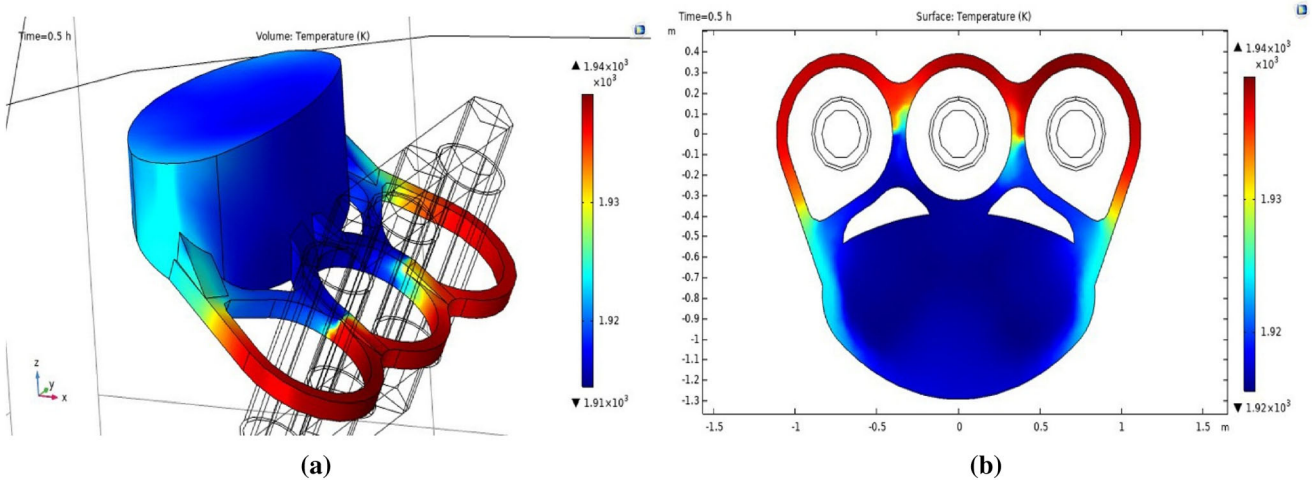


Figure 3. Temperature distribution of molten metal ($t = 0.5$ h): (a) 3D-temperature distribution, (b) Temperature distribution in middle section of channel according to $A_1B_1C_1D_1$.

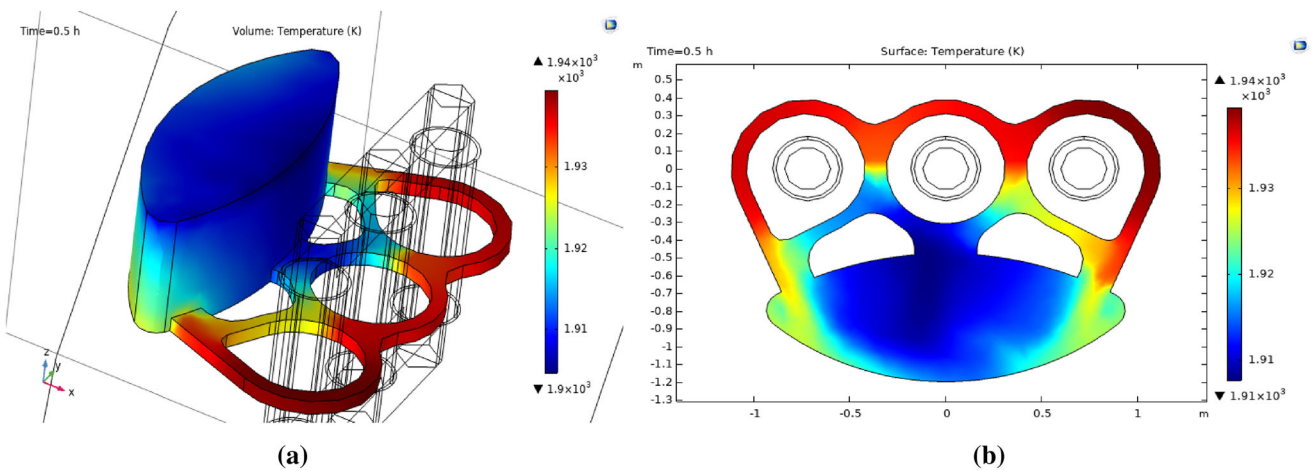


Figure 4. Temperature distribution of molten metal ($t = 0.5$ h): (a) 3D-temperature distribution, (b) Temperature distribution in middle section of channel according to $A_1B_2C_2D_2$.

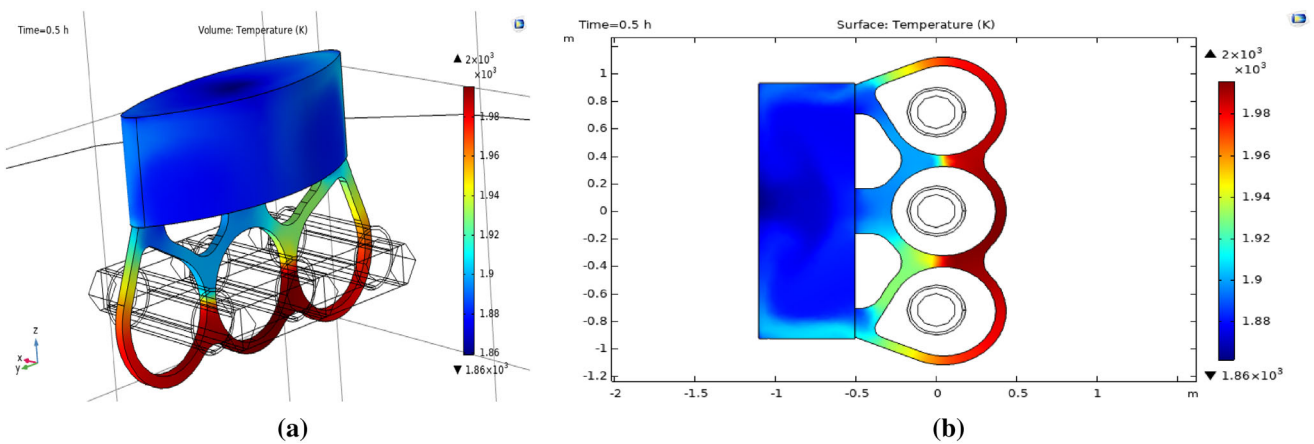


Figure 5. Temperature distribution of molten metal ($t = 0.5$ h): (a) 3D-temperature distribution, (b) Temperature distribution in middle section of channel according to $A_1B_3C_3D_3$.

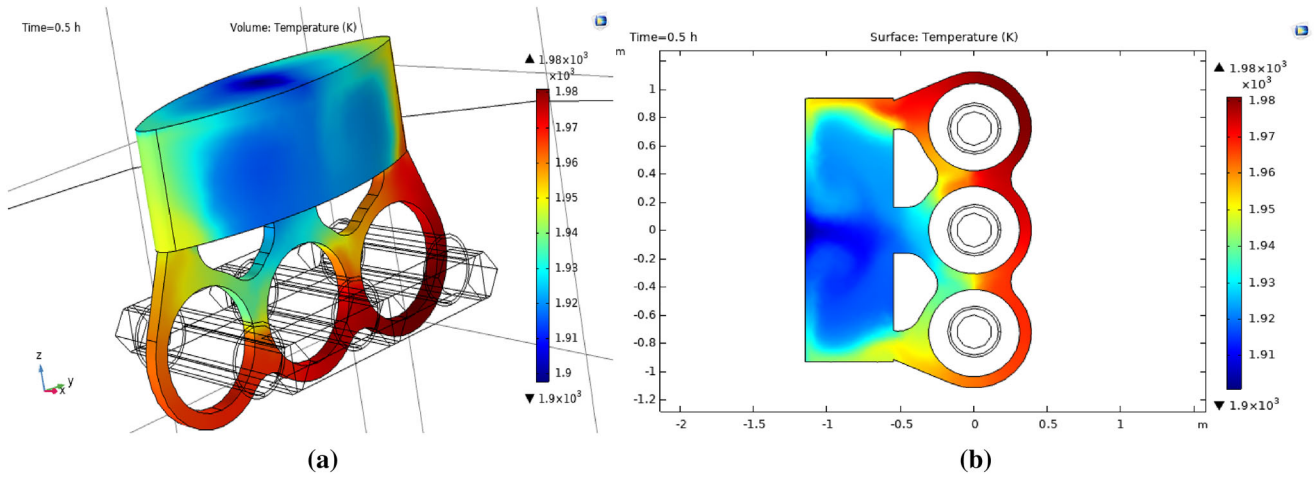


Figure 6. Temperature distribution of molten metal ($t = 0.5$ h): (a) 3D-temperature distribution, (b) Temperature distribution in middle section of channel according to $A_2B_1C_2D_3$.

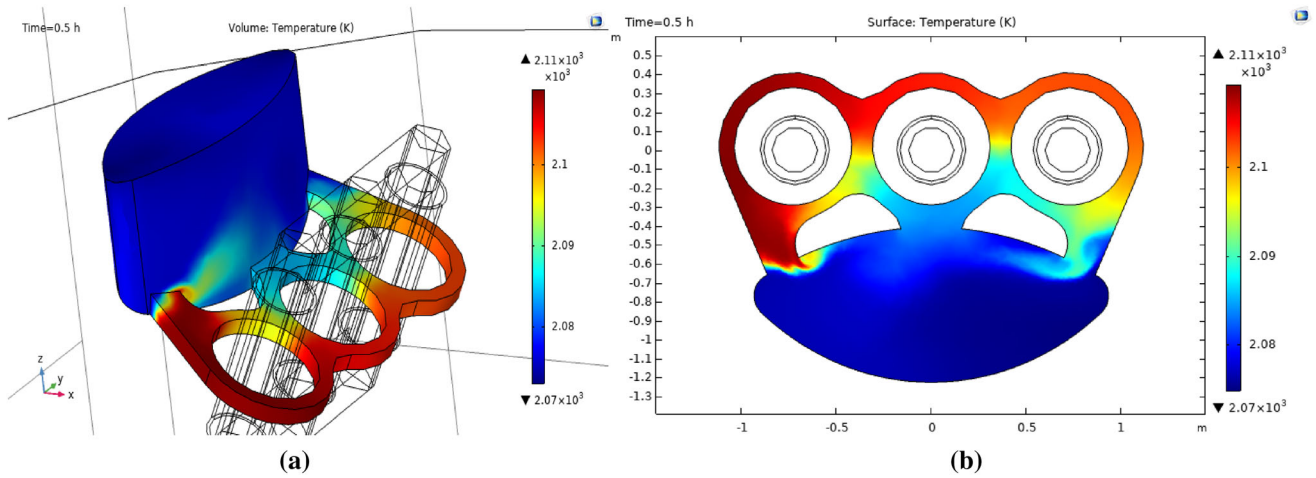


Figure 7. Temperature distribution of molten metal ($t = 0.5$ h): (a) 3D-temperature distribution, (b) Temperature distribution in middle section of channel according to $A_2B_2C_3D_1$.

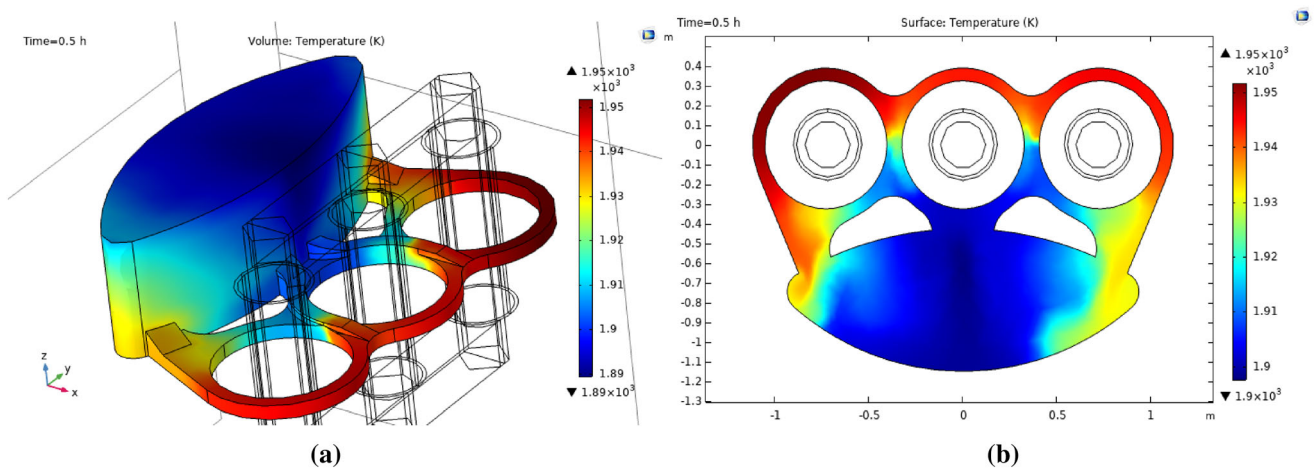


Figure 8. Temperature distribution of molten metal ($t = 0.5$ h): (a) 3D-temperature distribution, (b) Temperature distribution in middle section of channel according to $A_2B_3C_1D_2$.

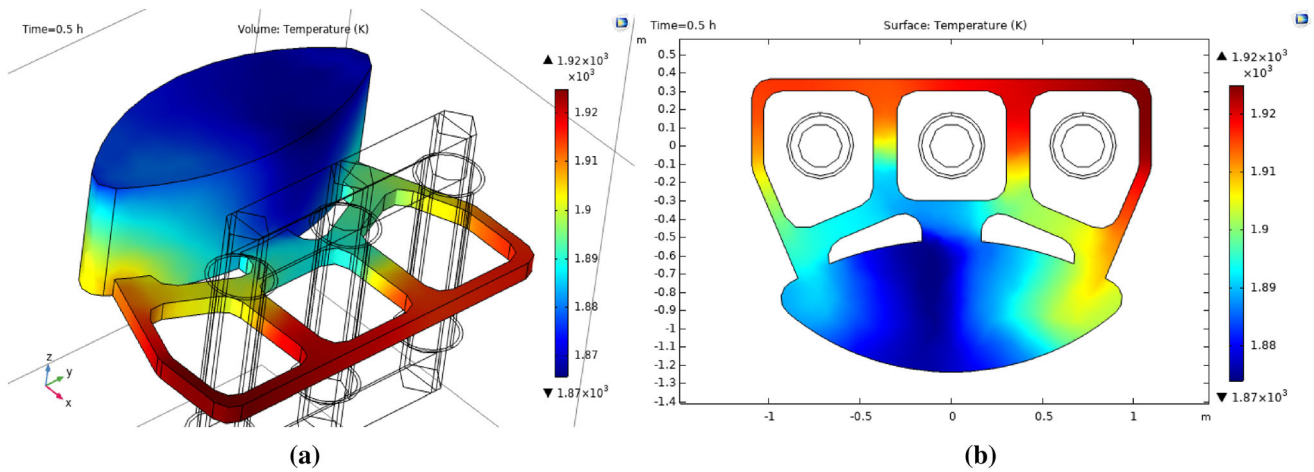


Figure 9. Temperature distribution of molten metal ($t = 0.5$ h): (a) 3D-temperature distribution, (b) Temperature distribution in middle section of channel according to $A_3B_1C_3D_2$.

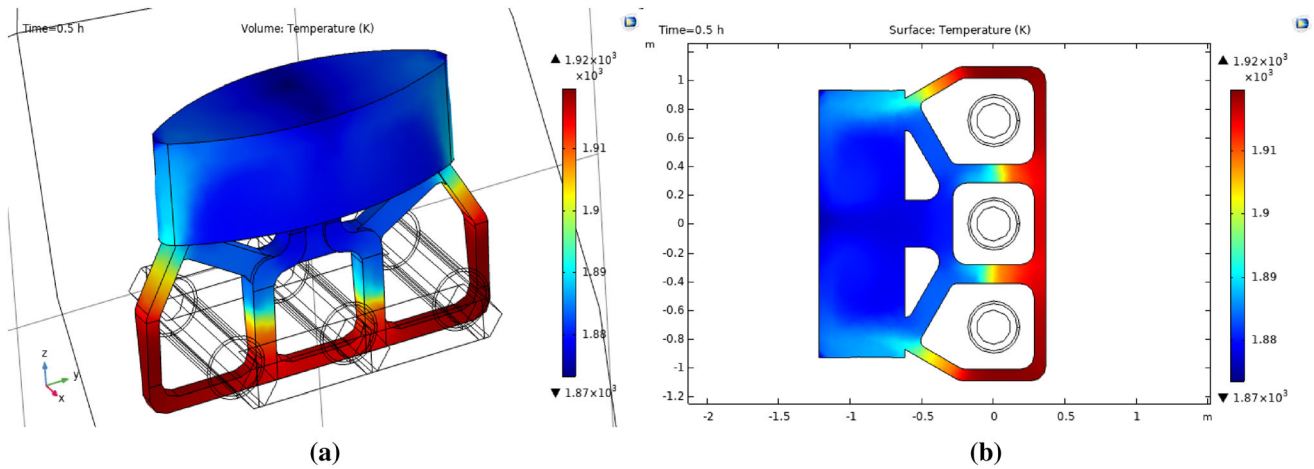


Figure 10. Temperature distribution of molten metal ($t = 0.5$ h): (a) 3D-temperature distribution, (b) Temperature distribution in middle section of channel according to $A_3B_2C_1D_3$.

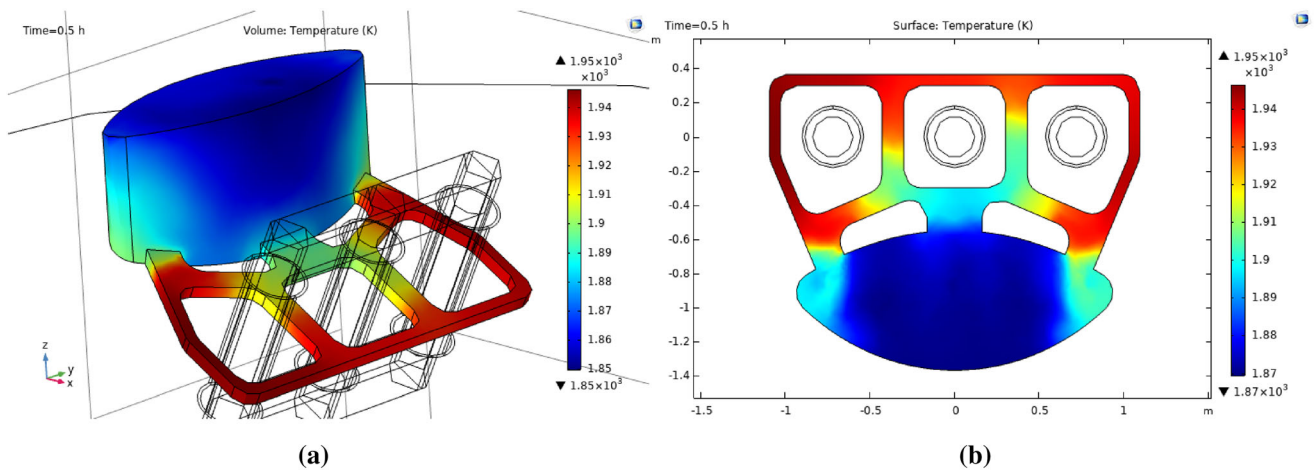


Figure 11. Temperature distribution of molten metal ($t = 0.5$ h): (a) 3D-temperature distribution, (b) Temperature distribution in middle section of channel according to $A_3B_3C_2D_1$.

In Figure 12, the horizontal axis indicates the level number of the factor and the vertical axis indicates the average values of S/N ratios. For example, the first graph of Figure 12 shows the average values of S/N ratios of the factor A (type of channel) at the levels 1–3., the coordinates of three points are, respectively, (1, -8.2730), (2, -9.1928) and (3, -10.4874).

Table 12. Simulation Experiment Results (Relative Local Superheating Temperatures, %) Based on the OA $L_9(3^4)$

Trial no.	Factor				Time t, h				
	A	B	C	D	0.1	0.2	0.3	0.4	0.5
1	1	1	1	1	1.538	1.456	1.383	1.327	1.279
2	1	2	2	2	1.828	1.823	1.809	1.806	1.805
3	1	3	3	3	6.877	6.883	6.863	6.845	6.826
4	2	1	2	3	4.176	4.191	4.188	4.198	4.205
5	2	2	3	1	1.825	1.787	1.764	1.745	1.721
6	2	3	1	2	3.265	3.246	3.224	3.21	3.192
7	3	1	3	2	3.084	3.106	3.093	3.081	3.081
8	3	2	1	3	2.451	2.448	2.435	2.433	2.417
9	3	3	2	1	4.949	4.987	4.981	4.971	4.968

Table 13. S/N Ratios for Each of Nine Trial Conditions

	A	B	C	D	SNR, dB
1	1	1	1	1	-2.9203
2	1	2	2	2	-5.1738
3	1	3	3	3	-16.725
4	2	1	2	3	-12.448
5	2	2	3	1	-4.9534
6	2	3	1	2	-10.1773
7	3	1	3	2	-9.7964
8	3	2	1	3	-7.7365
9	3	3	2	1	-13.929

Table 14. Average Values of S/N Ratios of Each Factor at Levels 1–3 and Their Ranges

	Level	Factor			
		A	B	C	D
Average value of S/N ratios	1	-8.2730	-8.3881	-6.9447	-7.2676
	2	-9.1928	-5.9546	-10.5169	-8.3825
	3	-10.4874	-13.6105	-10.4916	-12.3030
Range of S/N ratios (maximum-minimum)	2.2144	7.6560	3.5722	5.0354	
Rank	4	1	3	2	

Bold values indicate the maximum average values of S/N ratios for each factor. In Taguchi method, the optimal condition consists of the levels with maximum average values of S/N ratios for each factor

From Table 12 and Figure 12, it is clear that the average values of S/N ratios is maximized (the relative local superheating temperature is minimized) at the first level of factors A, C and D and at the second level of factor B. Therefore, the best condition (best levels) for reducing the relative local superheating temperatures of the three-phase ICF are A1, B2, C1 and D1. It is also clear that factors B and D are more prominent than other factors because their ranges of S/N ratios are larger than others.

It must be noted that the above combination of factorial levels (1, 2, 1, 1) was not one of the nine combinations tested in our set of simulation experiments based on the OA $L_9(3^4)$. This was expected because of the small number of simulation experiments conducted in the employed experimental design (9 from $3^4=81$ possible combinations).

As the result, the optimal design parameters (with maximum S/N ratio) for three-phase ICF are as follows:

- Type of channel: Elliptic
- Dimensions of channel: $85 \times 90 \text{ mm}^2$
- Existence of protruding part: Yes
- Setting angle of channel: 30° .

Confirmation Experiment Result According to the Best Condition $A_1B_2C_1D_1$

The obtained optimal design parameters (using best condition $A_1B_2C_1D_1$; Type of channel: Elliptic, Dimensions of channel: $85 \times 90 \text{ mm}^2$, Existence of protruding part: Yes, Setting angle of channel: 30°) are used for confirmation experiment.

Table 15 shows the maximum and minimum temperatures, and absolute and relative local superheating temperatures depending on time according to best condition $A_1B_2C_1D_1$.

Figure 13 shows the temperature distribution of the molten metal at the time $t = 0.5h$ according to best condition $A_1B_2C_1D_1$.

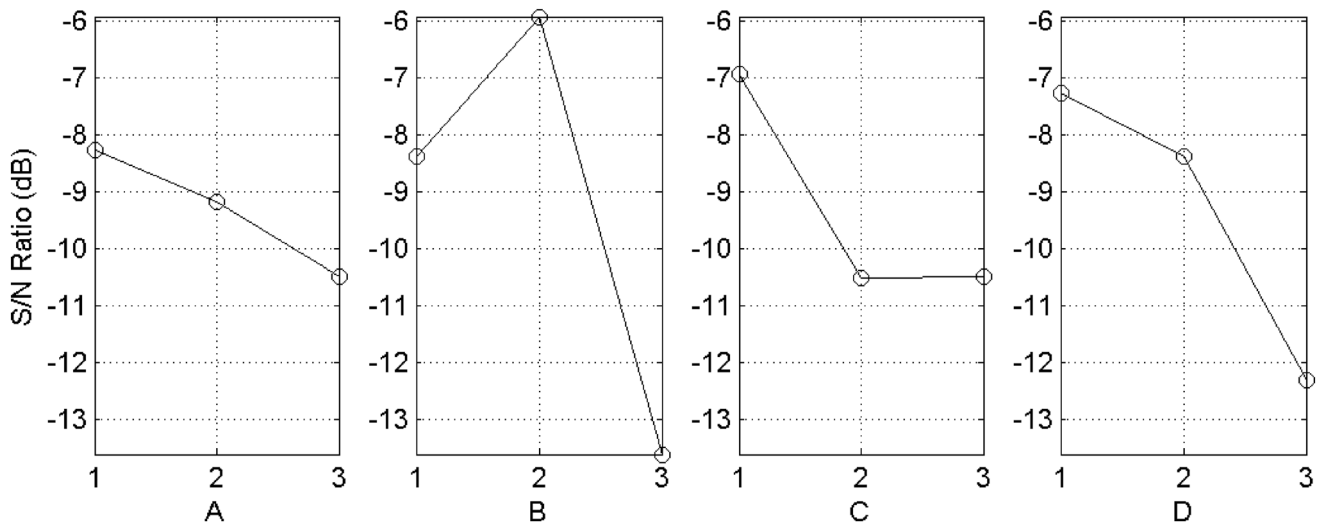


Figure 12. Average values of S/N ratios of each factor at levels 1–3.

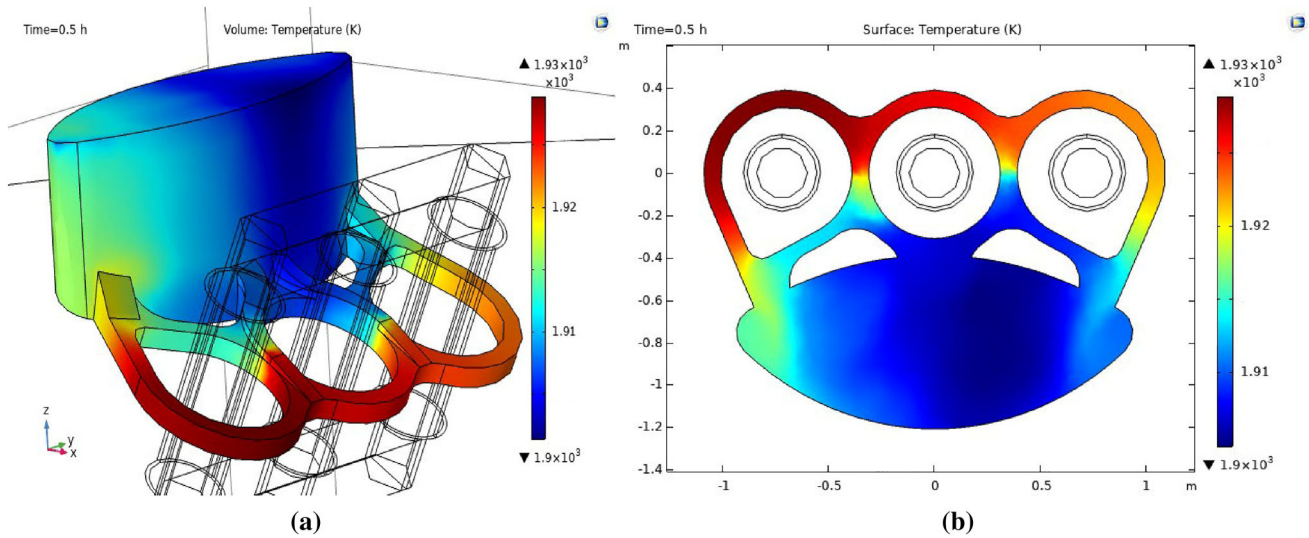


Figure 13. Temperature distribution of molten metal ($t = 0.5$ h): (a) 3D-temperature distribution, (b) Temperature distribution in middle section of channel according to best condition $A_1B_2C_1D_1$.

Table 15. Maximum and Minimum Temperatures, Absolute and Relative Local Superheating Temperatures Depending on Time According to Best Condition $A_1B_2C_1D_1$

Time t , h	0	0.1	0.2	0.3	0.4	0.5
Maximum temperature T_{max} , K	1811.2	1875.5	1894.1	1906.1	1914.9	1926.2
Minimum temperature T_{min} , K	1811.2	1854.7	1872.5	1883.3	1892.1	1903.3
Absolute local superheating temperature ΔT , K	0	20.8	21.6	22.8	22.8	22.9
Relative local superheating temperature δ , %	0	1.121	1.154	1.211	1.205	1.203



Figure 14. Channel and molten metal bath, and the photograph of our ICF in industrial application.

Table 16. Grain Composition of Refractory

Grain size of refractory, mm	<0.1	0.1~0.5	0.5~1	1~3	3~10	10~30
Content, %	25	20	15	15	15	10

The furnace that build and operate in industrial application shown in Figure 14 includes technical characteristics as shown in Table 17

Table 15 shows that the local superheating temperatures are, respectively, 20.8, 21.6, 22.8, 22.8, and 22.9, and the relative local superheating temperatures are, respectively, 1.121, 1.154, 1.211, 1.205, and 1.203.

Compared with Tables 12, 15 demonstrate that the design parameters according to the best condition $A_1B_2C_1D_1$ are very effective to minimize the local superheating temperature of the channel.

As shown in Table 15 and Figure 13, the local superheating temperature is relatively low as 20.8–22.9K and the maximum local superheating temperature 22.9K is similar to the maximum local superheating temperature 33K in channel of the Twin channel induction furnaces.⁷ In our opinion, the reason why the local superheating temperature become lower than one of the literature are as follows.

Firstly, the flow speed of molten metal in channel become quickly a little than other three-phase channel. The molten metal of the channel flows from center throat to side throats by force of hydrodynamical energy caused by geometric

character. In the literature⁷, the flow of molten metal have been observed in the jet flow type TCIF. Likewise, the flow molten metal of our channel is also observed in the jet flow type and so the local superheating temperature become lower.

Secondly the heat transfer condition of channel is more improved than other three-phase channel. Our channel have larger cross-sectional area than other channel of the literatures, and so the local superheating temperature become lower.

It is one of the ways to prevent the early erosion and expansion of refractory lining by local superheating in the channel and to increase the repair cycle.

One three-phase induction unit is fixed to the furnace body with the angle 30°, so the repair work of the furnace is easy. However, the furnace has a defect that the refractory consumption increases because the channel volume is bigger than the other ICFs.

We used the fused magnesia clinker and harden it by impact compactor in furnace body

Table 16 shows the grain composition of hardened refractory.

Practical Verification of the New Developed Three-Phase ICF

In order to verify the accuracy of simulation in three-phase ICF introduced and operated in the industry practice, the measurement experiment for temperature on the channel is conducted.

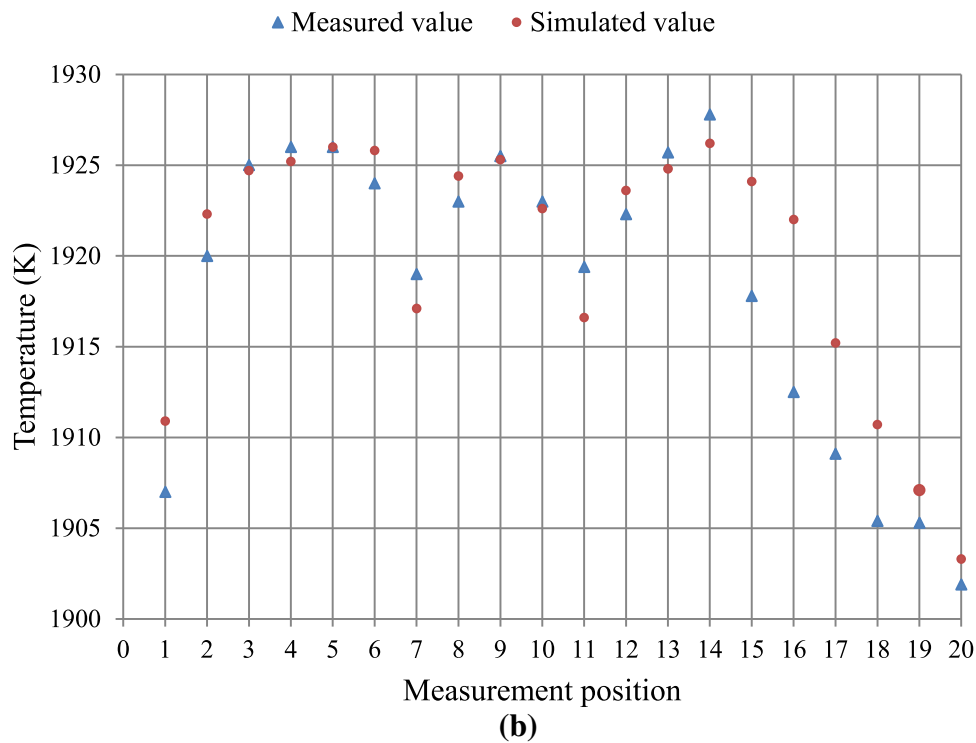
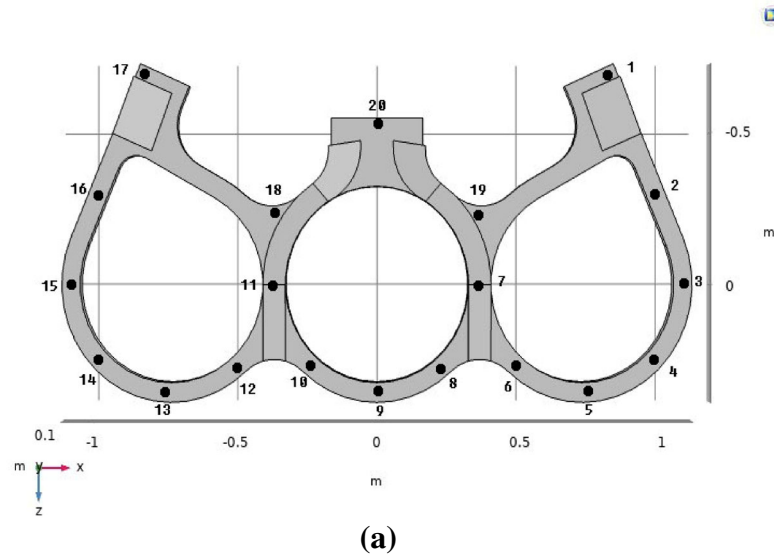


Figure 15. Temperature measurement position on channel (a) and measured and simulated values of temperature on the measurement positions (b).

Figure 15 shows the temperature measurement positions on the channel and the graph of the measured and simulated values of the temperature on the measurement positions.

As shown in Figure 15b, the temperature of the back side of the channel is higher than the temperature of the part connected with the molten metal bath in the industrial three-phase ICF for steel casting and the local superheating temperature (25.9 K) from the experiment is slightly larger (3 K) than the simulation result (22.9 K). The difference is

acceptable if we take into account the assumptions made in the calculations.

Conclusion

In this paper, a new type of channel of three-phase ICF for steel melting was proposed, and its temperature distribution analysis was conducted by coupled simulation of the electromagnetic-heat-fluid multiphysics field using COM-SOL Multiphysics 5.4 and Taguchi method. The

Table 17. Technical Characteristics of Furnace

Item	Unit	Value
Melting quantities per charge	t	2
Melting time	h	3
Primary voltage	kV	3
Secondary Voltage step	V	200, 300, 400, 500, 600, 700
Maximum current	A	600
Power factor ($\cos\phi$)	Original power factor	0.7
	Compensation power factor (with condenser)	0.95
Rated power	kW	500
Condenser	kVAr	300 (3 000 μ F, dielectric breakdown voltage 1 000 V)
Electric power consumption	kWh/	650
	t	
Output temperature of cooling water	$^{\circ}$ C	≤ 40
Melting cost	\$/t	70

temperature and velocity distributions in channel depend on the channel geometry, placement relationship of the channel and the molten metal bath, and electric parameters in the ICF.

We have proposed a new type channel of three-phase ICF for steel melting, and suggested the method for simulating heating and melting process by electromagnetic field and Joule heat and flow characteristics of molten metal by gravity and Ampere force on the channel by using COM-SOL Multiphysics5.4. The simulation results on temperature field distribution demonstrate that the local superheating temperature in channel of three-phase ICF for steel melting is similar to that of channel of two phase ICF (27–33 K) as 28.6 K. When simulating the velocity of molten metal flowing in channel by gravity and Ampere force, the velocity is 0.721 m/s in upper part of entrance of central channel of which flow velocity is fastest, and then we could find that is to ensure the velocity of molten metal sufficiently and to high translocation flow velocity comparative in channel.

The method could be used to decrease the manufacture cost and regularizing operation through optimizing the parameters of induction furnace needed in aimed melting and flow.

Acknowledgements

This work was supported by Kim Chaek University of Technology, Democratic People's Republic of Korea.

The supports are gratefully acknowledged. The authors thank to the editors and reviewers for their helpful suggestions for improvement and publication of this manuscript.

Data Availability

All data that support the findings of this study are included within this article.

Conflict of interest The authors declared no potential conflicts of interest with respect to the research, authorship, and publication of this article.

REFERENCES

1. V.R. Gandhewar, S.V. Bansod, A.B. Borade, Induction furnace - a review. *Int. J. Eng. Technol.* **3**(4), 277–284 (2011)
2. E. R. Webster Jr, Improved Method for Lining Channel Furnace Inductors, AFS Transactions 01-101, Blasch Precision Ceramics, Albany, New York
3. E. Calamari, Induction furnace with incorporated channel. *AFS Trans.* **70**, 1243–1248 (1962)
4. W.J. Duca, Thermodynamics of Inductor Saturation, *Modern Casting*, Aug 1995, 32–34
5. W.J. Duca, How treated ductile iron returns contribute to channel furnace inductor lining wear – part II. *AFS Trans.* **119**, 497–500 (2011)

6. N. Bara, Review paper on numerical analysis of induction furnace. *Int. J. Latest Trends Eng. Technol. (IJLTET)* **2**(3), 178–184 (2013)
7. J.I. Ghojel, Thermal analysis of twin-channel induction furnace. *Metall. Mater. Trans. B.* **34B**, 679–684 (2003)
8. J.I. Ghojel, R.N. Ibrahim, WITHDRAWN: Computer simulation of the thermal regime of double-loop channel induction furnaces. *J. Mater. Process. Technol.* **155–156**, 2093–2098 (2004)
9. A. Alferenok, A. B. Kuvaldin, Numerical simulation of the heat-and-mass transfer in the channel of an induction furnace for making cast iron, *Russian Metallurgy (Metally)*, No. 8, 2009, 741–747.
10. S. Pavlovs, A. Jakovics, D. Bosnyaks, B. Nacke, E. Baake, Anomalies of Joule heat, thermal and turbulent flow field in clogged industrial channel induction furnaces, *HES-13-International Conference on Heating by Electromagnetic Sources*, May 21–24, 2013, Padua, Italy.
11. S. Pavlovs, A. Jakovics, D. Bosnyaks, E. Baake, B. Nacke, Turbulent flow, heat and mass exchange in industrial induction channel furnaces with various channel design, iron yoke position and clogging, *Conference Paper*, Sept 2012.
12. E. Baake, A. Jakovics, S. Pavlovs, M. Kirpo, Influence of the channel design on the heat and mass exchange of induction channel furnace. *The Int. J. Comput. Math. Electr. Electron. Eng.* **30**(5), 1637–1650 (2011)
13. A. Jakovics, S. Pavlovs, M. Kirpo, E. Baake, Long-term LES study of turbulent heat and mass exchange in the induction channel furnaces with various channel design, *Proceedings of 8th PAMIR International Conference on Fundamental and Applied MHD*, Sept 5–9, 2011, Borgo, France, Vol. 1, 283–288
14. M. Kirpo, A. Jakovics, E. Baake, B. Nacke, Analysis of heat and mass transfer processes in the melt of induction channel furnaces using LES. *Magnetohydrodynamics* **45**, 267–273 (2009)
15. E. Baake, A. Jakovics, S. Pavlovs, M. Kirpo, Long-term computations of turbulent flow and temperature field in the induction channel furnace with various channel design. *Magnetohydrodynamics* **46**, 461–474 (2010)
16. M. Langejürgen, M. Kirpo, A. Jakovics, R. Baake, Numerical simulation of mass and heat transport in induction channel furnaces, *International Scientific Colloquium Modelling for Electromagnet Processing*, Hannover, Oct 27–29, 2008
17. E. Baake, A. Jakovics, S. Pavlovs, M. Kirpo, Numerical analysis of turbulent flow and temperature field in induction channel furnace with various channel design, *International Scientific Colloquium, Modelling for Material Processing*, Riga, Sept 16–17, 2010.
18. M. Kirpo, A. Jakovics, B. Nacke, E. Baake, M. Langejürgen, LES of heat and mass exchange in induction channel furnaces, *Przegląd Elektrotechniczny*, ISSN 0033-2097, R.84 NR 11(2008) 154–158
19. A. D. Podoltsev, V. M. Zolotaryov, M. A. Shcherba, R. V. Belyanin, Calculation of the equivalent electrical parameters of the inductor of induction channel furnace with defects in its lining, *лектротехніка і Електромеханіка*, 2018, №4, 29–34
20. N. T. T. Hang, U. Lüdtke, Numerical simulation of induction channel furnace to investigate efficiency for low frequencies, *IOP Conf. Ser.: Mater. Sci. Eng.* **355**, (2018)
21. H. Singh, S. Dharonde, P. Saxena, U. Mishra, Y.M puri, A.M Kuthe, Finite element analysis of induction heating process design for SMART Foundry 2020, *COMSOL conference 2019*, Boston
22. A. A. Bhat, S. Agarwal, D. Sujish, B. Muralidharan, B.P. Reddy, G. Padmakumar, K.K.Rajan, Thermal analysis of induction furnace, *COMSOL Conference 2012*, Bangalore
23. I. Quintana, Z. Azpilgain, D. Pardo, I. Hurtado, Numerical modeling of cold crucible induction melting, *COMSOL Conference 2011*, Stuttgart
24. S. Ghorbanzadeh, M. Nazari, M.M. Shahmardan, A. Hasannia, Simultaneous numerical modelling of heat transfer and magnetic fields in a vacuum induction furnace. *Modares Mech Eng* **19**(4), 959–967 (2019)

Publisher's Note Springer Nature remains neutral with regard to jurisdictional claims in published maps and institutional affiliations.

Springer Nature or its licensor (e.g. a society or other partner) holds exclusive rights to this article under a publishing agreement with the author(s) or other rightsholder(s); author self-archiving of the accepted manuscript version of this article is solely governed by the terms of such publishing agreement and applicable law.